Experimental and analytical study of X-section cast-in-place concrete pile installation effect

Article *in* International Journal of Physical Modelling in Geotechnics · January 2017

DOI: 10.1680/jphmg.15.00037

5 authors, including:

Hang Zhou
Chongqing University
40 PUBLICATIONS **82** CITATIONS
SEE PROFILE

Gang-Qiang Kong
Hohai University
96 PUBLICATIONS **203** CITATIONS
SEE PROFILE

Zhaohu Cao
Hohai University
17 PUBLICATIONS **26** CITATIONS
SEE PROFILE

International Journal of Physical Modelling in Geotechnics

Experimental and analytical study of X-section cast-in-place concrete pile installation effect
Zhou, Liu, Randolph, Kong and Cao

International Journal of Physical Modelling in Geotechnics
http://dx.doi.org/10.1680/jphmg.15.00037
Paper 1500037
Received 26/09/2015 Accepted 02/12/2016
Keywords: design methods & aids/foundations/piles & piling

ice Institution of Civil Engineers
publishing

Experimental and analytical study of X-section cast-in-place concrete pile installation effect

Hang Zhou PhD
Lecturer, College of Civil Engineering, Key Laboratory of New Technology for Construction of Cities in Mountain Area, Chongqing University, Chongqing, China (corresponding author: zh4412517@163.com)

Hanlong Liu PhD
Professor, Key Laboratory of Ministry of Education for Geomechanics and Embankment Engineering, Hohai University, Nanjing, China

Mark F. Randolph FAA, FREng, FRS, FTSE, FIEAust, CPEng
Fugro Chair in Geotechnics, Centre for Offshore Foundation Systems, The University of Western Australia, Perth, Western Australia

Gangqiang Kong PhD
Associate Professor, College of Civil and Transportation Engineering, Key Laboratory of Ministry of Education for Geomechanics and Embankment Engineering, Hohai University, Nanjing, China

Zhaohu Cao PhD
PhD Candidate, College of Civil and Transportation Engineering, Key Laboratory of Ministry of Education for Geomechanics and Embankment Engineering, Hohai University, Nanjing, China

A new type of displacement pile, the X-section cast-in-place concrete (XCC) pile, has been developed recently in China. Extensive field and laboratory experiments are being undertaken in order to evaluate the soil displacements during pile installation. The paper describes laboratory arrangements and results of transparent soil model tests aimed at capturing the non-axisymmetric soil displacement field. Results from model tests using the XCC pile are presented to reveal the complete soil displacement patterns (a) in the horizontal plane, and (b) in vertical planes of symmetry. Based on results from the transparent soil tests, a modified cavity expansion model (MCEM) is proposed to predict the radial displacements in any vertical plane induced by XCC pile installation. The radial displacements predicted by the MCEM are compared with data from the transparent soil test and the field experiment. The results show reasonable agreement for all cases, with the proposed MCEM proving more suitable than the conventional (axisymmetric) CEM for predicting the radial displacements induced by XCC pile installation. It may therefore provide a basis in the future for developing predictions of stress changes and, ultimately, shaft capacity of the XCC pile in comparison to displacement piles of circular cross-section.

Notation

A_{xcc}	area of XCC pile cross-section.
a, b, θ_0	three parameters of XCC pile cross-section
C	constant coefficient
G	shear modulus of soil
L	penetration depth of the pile
r	radial position in pile cross-section plane
R	radius of the circular pile
R_{eq}	equivalent radius of the pile
R_t	radius of the transition zone
s_u	undrained strength of soil
u_r	radial displacement
$u_{rb}(\theta)$	radial displacement at the pile–soil interface
u_{rt}	radial displacement at boundary of the transition zone
u_z	vertical displacement
z	depth of soil
ε_r, ε_θ	radial and circumferential strain
ε_v	volume strain
θ	polar angle in pile cross-section plane
θ	polar angle in pile cross-section plane
v	Poisson's ratio of soil

1. Introduction

Quantifying the soil movements due to installation of displacement piles is important for assessing potential damage to adjacent structures, and also as a basis for estimating the eventual shaft capacity. Physical modelling has played an important role in predicting soil displacement around piles. Early work (Gue, 1984; Randolph *et al.*, 1979) reported model pile tests in kaolin contained in semicircular containers, with markers placed on a cross-section behind a viewing window tracked by photography. This was sufficient for axially symmetric pile geometries, but would not allow measurement of the internal displacement field for piles of more complex shapes.

Internal imaging techniques to visualise flow and deformation within the soil body have included radiography (X-ray, γ-ray), computerised axial tomography (CT) and nuclear magnetic resonance imaging (Lorenz and Heinz, 1969; Mandava *et al.*, 1990; Orsi *et al.*, 1992; Posadas *et al.*, 1996; Roscoe *et al.*, 1963). However, routine application of these techniques is limited mainly by the high cost of the experimental set-up and also by their technical limitations.

A much simpler technique is possible using the transparent synthetic material developed by Iskander *et al.* (1994). The material, which comprises amorphous silica particles and a pore fluid with an accurately matched refractive index, is almost transparent and has geotechnical properties similar to those of clay. 'Transparent soil' of this type was used in model pile tests by Lehane and Gill (2004). During the model pile installation, the displacement paths of black spherical beads embedded in the soil were recorded by a video camera. However, the use of embedded markers restricts displacement measurement to discrete points, rather than throughout the full soil domain.

To resolve this problem, laser technology (Liu and Iskander, 2004; Sadek *et al.*, 2003) may be combined with particle image velocimetry (PIV) (White *et al.*, 2003), as described by Ni *et al.* (2010) for cylindrical piles jacked into a transparent medium and Hird *et al.* (2011) for augered piles. Similar techniques are now being used widely in geotechnical research.

2. Definition of the XCC pile

A new type of displacement pile, the XCC pile, has been developed recently in China. This type of pile has been used for soft ground improvement during highway and railway construction (Liu *et al.*, 2014; Lv *et al.*, 2014a, 2014b). The special 'X' cross-section shape creates a pile with larger side surface per unit volume than for a conventional cylindrical or square pile. It also allows the pile to be vibratory driven into place relatively easily, in combination with applied static force. This type of pile is formally classified as a 'cast-in-situ' displacement pile. This is a well-established construction technique that tends to give higher capacity than a pure (e.g. precast concrete or steel) displacement pile, mainly due to improved frictional transfer along the rough shaft. The installation of the pile casing causes outward displacement of the surrounding soil. Although there will be some stress (and displacement) relaxation as the pile is cast, with the pile casing being extracted, the inward soil movement is relatively small and elastic. In common with other cast-in-situ displacement piles, the soil does not become mixed with the concrete during extraction of the casing since the casing is vibrated out gradually, while ensuring that the concrete fills the X-shaped hole completely. Excavation of the XCC pile in the field has shown that the final form of the XCC pile body is consistent with the shape of the casing (Figure 2). Typical volumes of concrete, relative to the gross volume of the casing, are between 1 and 1·25 (Lv *et al.*, 2011). The study presented here is a contribution towards, although not the final solution for, developing a scientific basis for estimating the axial response of such piles, by comparison with piles of circular cross-section.

Figure 1 shows a cross-section of the XCC pile, which contains four flat and four cambered sections. The centres of each cambered section are located at points such as *O*. Three parameters a, b, θ_0 are used to control the size and shape of the XCC pile cross-section. Parameter a gives the diagonal distance between two opposite flat sections; parameter b is the length of each flat section, while θ_0 defines the angle of the cambered section. In practice, four geometries are commonly used for XCC pile, as detailed in Table 1.

Figure 2 shows typical XCC piles in the field. They are cast in situ and are installed by: (*a*) vibratory driving the X-shaped cross-section pile mould (Figure 3) into the soft soil; (*b*) pouring concrete into the mould; and by (*c*) extracting the pile mould.

3. Objectives

In this paper, the transparent soil technology and PIV technique are used to investigate the soil displacement field induced by XCC pile installation. A model pile, which is used to simulate the X-shaped cross-section pile mould, is penetrated into the transparent soil. The soil displacement field was evaluated for both penetration and extraction of the model XCC pile, although the present paper deals only with the penetration phase, which had a much greater influence on the surrounding soil. Subsequently, based on results from transparent soil tests, a modified cavity expansion model (MCEM) is proposed to predict the radial displacements in any vertical plane induced by XCC pile installation.

Radial displacements measured in a field test are also presented. The radial displacements predicted by the MCEM are

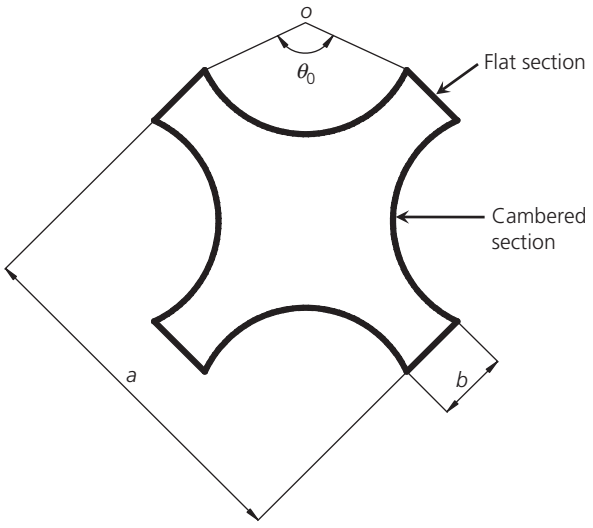

Figure 1. XCC pile cross-section

Table 1. XCC pile cross-section parameters

Case	*a*: mm	*b*: mm	θ_0: deg
1	530	110	90
2	530	110	130
3	611	120	90
4	611	120	130

Figure 2. Typical XCC pile in the field

compared with data from both the model test in transparent soil and the field experiment. Reasonable agreement is shown in both cases, with the proposed MCEM proving more suitable than a simple axisymmetric cavity expansion method (CEM) for predicting the radial displacements induced by XCC pile installation. It may therefore provide a basis in the future for developing predictions of stress changes and, ultimately, shaft capacity of the XCC pile in comparison to displacement piles of circular cross-section.

4. Evaluation of pile installation effect

The soil displacement field and the resulting stress changes in the soil arising from installation of cylindrical piles have typically been evaluated by two approaches: (*a*) CEM (Cao *et al.*, 2001; Carter *et al.*, 1986; Chen and Abousleiman, 2012; Gibson and Anderson, 1961; Hill, 1950; Randolph *et al.*, 1979; Salgado *et al.*, 1997; Vesic, 1972; Yu, 1990; Zhou *et al.*, 2014a, 2014b, 2014c, 2015) and (*b*) shallow strain path method (SSPM) (Baligh, 1985; Sagaseta *et al.*, 1997).

4.1 CEM

The CEM, as applied to piles, assumes that pile installation gives rise to radially outward displacement of the soil, with a strain field that resembles spherical cavity expansion ahead of the pile tip, with a transition to cylindrical cavity expansion around the pile shaft. In the latter case, due to radial symmetry, all the field variables (i.e. displacements, strains, stresses and pore pressures) depend only on the radial distance from

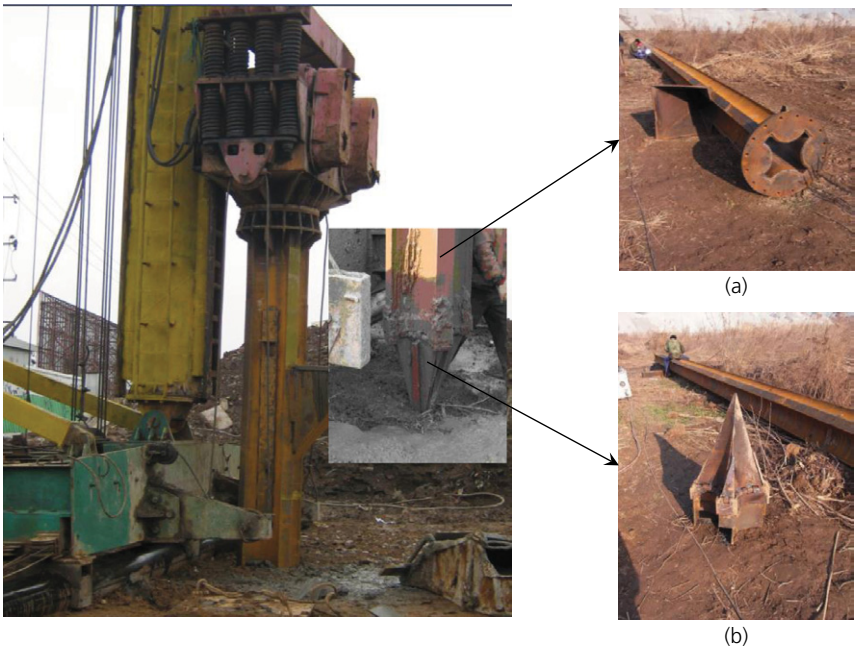

Figure 3. (a) XCC pile mould and (b) conical shoe with similar cross-section

the pile axis. Randolph *et al*. (1979) showed that the CEM provides a reasonable estimate of the radial displacements induced during penetration of a cylindrical displacement pile. The CEM expression for the radial displacement, u_r, for soil at final radius, r, is given by

$$1. \quad \frac{u_r}{R_{eq}} = \frac{r}{R_{eq}} - \sqrt{\left(\frac{r}{R_{eq}}\right)^2 - 1}$$

where R_{eq} is the pile radius for a closed-ended pile or the radius of an equivalent solid pile that gives the same volume of displaced soil for an open-ended pile. For an XCC pile, the equivalent radius would be

$$2a. \quad R_{eq} = \sqrt{\frac{A_{xcc}}{\pi}}$$

$$2b. \quad A_{XCC} = \frac{a^2 - 2b^2 + 2b\sqrt{a^2 - b^2}}{2} - \left(a^2 - 2b\sqrt{a^2 - b^2}\right)\frac{\theta - \sin\theta}{4\sin^2(\theta/2)}$$

where A_{xcc} is the area of the XCC pile cross-section.

4.2 SSPM

SSPM, widely used to model the effect of pile installation, is an extension of the strain path method (SPM) developed by Baligh (1985). During pile penetration, the soil is assumed to 'flow' around the advancing pile in a manner similar to an incompressible inviscid fluid, with the flow field independent of the shearing resistance of soil. The strain path for each soil element is obtained by integrating along the flow streamlines. Then the cumulative strain is used to estimate changes in effective stress for the given constitutive model of soil. The SSPM proposed by Sagaseta *et al*. (1997) modified the SPM by allowing for the influence of the free ground surface on the soil response.

5. Experimental programme

5.1 Transparent soil

The transparent soil used in this study is made of fused silica (Ezzein and Bathurst, 2011) with a blend of two mineral oils. As shown in Figure 4, the fused silica was with an aggregate diameter of 0·5–1 mm and angular particle shape. The detailed properties of fused silica are summarised in Table 2. The fused silica (from Jiangsu Kaidai Silica Co., Ltd, China) was saturated with a mixture of two mineral oils: N-dodecane (from Fushunbeiyuan Co., Ltd, China) and Whiter oil ISO 15 (from Shanghai Eastern Biz Co., Ltd, China). Several tests were devised to find an optimum oil blend to provide the best match to the refractive index of the silica powder, using an Abbe refractometer. For a ratio of the N-dodecane to Whiter oil ISO 15 of 1:4 by weight; the refractive index of the mixed oils was 1·458 at 20°C, which is consistent with that of fused silica. Hence, a ratio of 1:4 by weight was used to make the transparent soil for all tests reported here. Even small temperature changes can significantly affect the refractive index and hence the soil transparency; hence tests were conducted in an air-conditioned room where the temperature was kept constant to within ±1°C (Guzman and Iskander, 2013; Ni *et al*., 2010).

Before mixing the soil sample it was important to clean and dry thoroughly all beakers, dishes and boxes used in the sample preparation process (Welker *et al*., 1999). The blended oil was poured into the Perspex box 340 mm long, 170 mm wide and 250 mm tall. The dimensions of the model were

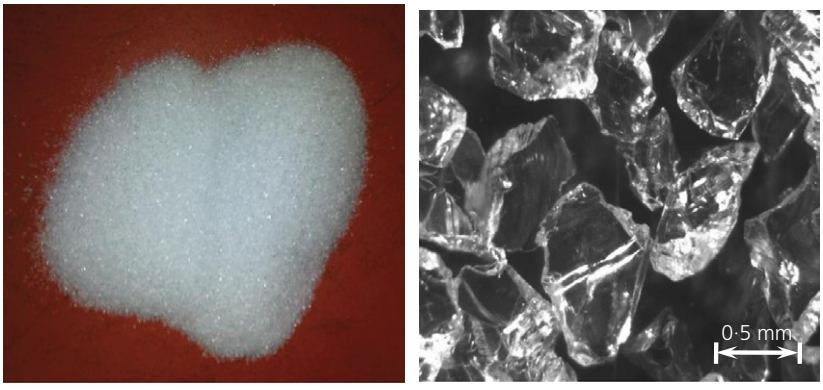

(a) (b)

Figure 4. (a) Fused silica particle and (b) electron microscope image

Table 2. Properties of fused silica

Property	Value
Specific gravity	2·186
Friction angle	50 to 54°
Particle size range	0·5–1 mm
Particle shape	Angular
Modulus of elasticity	30 MPa
Cohesion	0

chosen in such a way that boundary effects were minimised and yet the transparency of the soils was still sufficient for the camera to capture the speckle pattern within the 'soil'. Then the fused silica was poured gradually into the Perspex box from about 100 mm above the oil surface to avoid air being trapped in voids between the particles. A whisk was used to stir the slurry to ensure thorough mixing.

Once in place, the transparent soil was left to stand for a period of 3–5 d, during which time it is likely to have developed some shear strength. No attempts were made to quantify the shear strength of the soil, or the extent to which volumetric strains might occur during installation of the model pile. The relatively large grain size of the fused silica renders its response more like sand than clay, although this is compensated by the highly viscous nature of the oil (two to three orders of magnitude greater than water). As will be shown later, displacement patterns obtained following installation of a cylindrical model pile agreed well with theoretical predictions based on constant volume conditions. As such, given that the primary objective of the model tests was to quantify the asymmetric pattern of soil displacements arising from the shape of the XCC cross-section, the strain response of the fused silica was considered adequate, with conditions close to constant volume within the bulk of the soil. The surface of the soil was left unconfined, simulating the free surface of the ground in prototype conditions, since the authors were interested in full three-dimensional soil displacements, not just a planar idealisation.

Figure 5 shows the transparent soil sample, which has sufficient transparency to see the words behind the Perspex box. In addition, Figures 5(b) and 5(c) show that the laser-induced speckle pattern in this test has good quality with the light spots (used for PIV processing) having quite uniform distribution in the transparent soil without additional reflective particles, other than the fused silica itself.

5.2 Model pile

Test were undertaken using three different model piles: (*a*) cylindrical with flat pile tip, (*b*) cylindrical with 60° conical tip, (*c*) XCC model with 60° conical tip (Figure 6). The length of the four model piles was 200 mm. They were all made of aluminium alloy with dark colour to reduce light reflection. The XCC pile shaft contains two sections: flat and cambered sections. The radius of the circular model pile was 10 mm, while the three cross-section parameters of the XCC model pile were $a = 29$ mm, $b = 5{\cdot}5$ mm, $\theta_0 = 130°$. These dimensions lead to a cross-sectional area of $A_{XCC} = 305$ mm^2, and hence an equivalent pile radius, R_{eq} of 9·9 mm ($= 0{\cdot}35a$). The tops of the model piles have a connector, which was attached to a drive shaft. In turn, the shaft was controlled by a stepper motor turning a lead screw to give a vertical penetration speed of 1 mm/s.

It is believed that the presence of the (very viscous) oil rendered the 'soil' response close to undrained during insertion of the pile, also moderating significant pile-particle scaling effects. The large particle size may have led to some distortion of the near-field displacements, but the pattern in the far field should be largely unaffected. Note that the model pile surface was deliberately roughened, with maximum roughness R_t of about 1 mm (giving a normalised roughness ratio of $R_n = R_t/D_{50} \sim 1{\cdot}4$). The roughness would have a limited effect on the displacements induced by pile penetration, apart from very close to the pile shaft, although it would naturally affect the shaft resistance, which is outside the scope of this paper.

5.3 Test set-up

The test set-up is shown in Figure 7. The test was performed in a dark room on an optical platform 1800 mm long, 1200 mm wide and 750 mm above floor level, on which the test set-up could be positioned precisely. A 2 W semiconductor laser was adopted in the test to produce a light beam that spreads into a vertical light sheet of uniform intensity, illuminating a plane inside the soil sample. The model piles were driven at the centre of the sample, and a vertical light sheet was aligned with the pile axis. As the light sheet could not go beyond the pile, only half the soil model could be photographed usefully. Additionally, the set-up also included a charge-coupled device (CCD) camera and a computer for image processing. The camera had a resolution of 1280×960 pixels and was controlled by the computer through Matrox Meteor 2/4 frame grabber. It was important to ensure that the camera was positioned perpendicular and central to the plane of measurement to avoid any parallax effect (Ahmed and Iskander, 2010).

5.4 Image processing and PIV

The registered images were analysed using PIVview software (Willert, 2015: PIVview 2C/3C User Manual Version 2.3), which is a compact program package for the evaluation of PIV or speckle displacement recordings. It is known that the interaction between laser light and transparent soils produces a distinctive speckle pattern. This speckle pattern manifests the interactions between the laser and the transparent soil matrix, impurities and entrapped air. Small particle movements result in a change in speckle distribution in the plane of

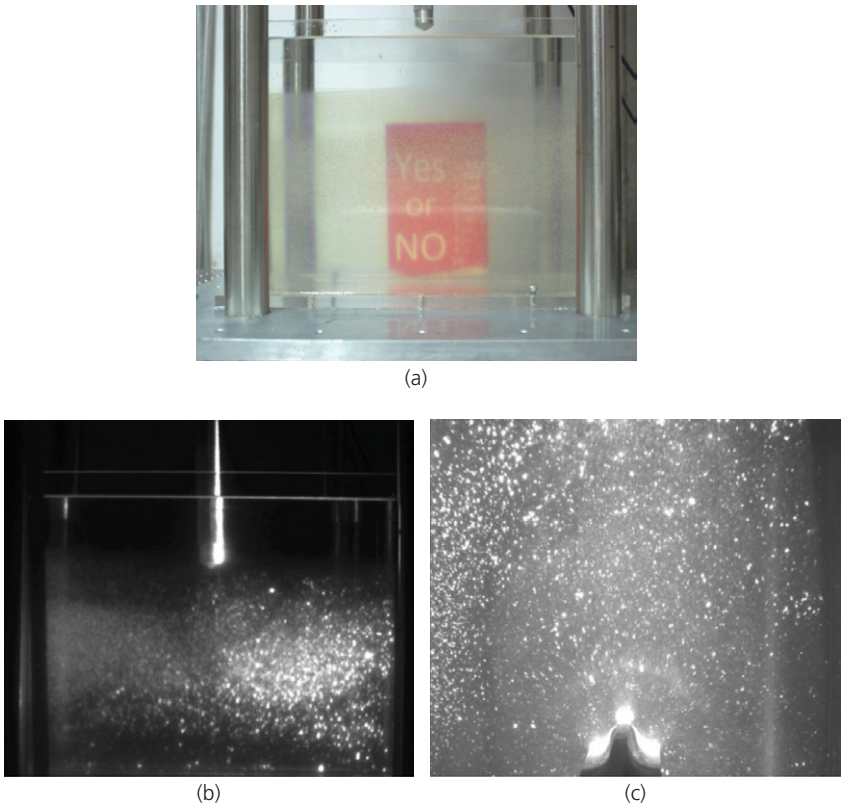

Figure 5. (a) Transparent soil sample, (b) laser-induced speckle pattern in the vertical plane, (c) laser-induced speckle pattern in the horizontal plane

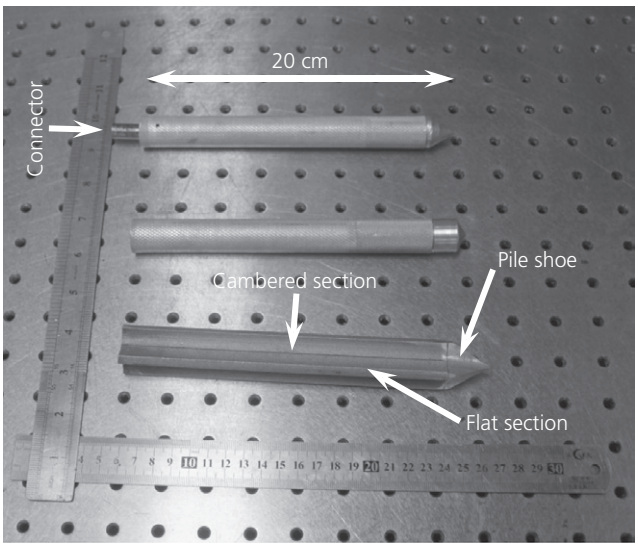

Figure 6. Model piles

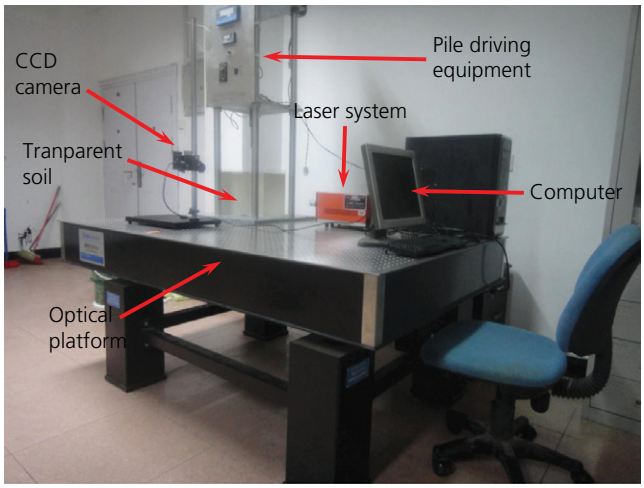

Figure 7. Test set-up for XCC pile penetration into transparent soil

measurement. If the deformation is small, good contrast distribution can be achieved between sequential images.

PIVview was able to capture images before and after pile penetration in order to measure the resulting displacements and (ultimately) strains within the soil. A mesh of square patches was drawn in the area of interest on an initial image, and the locations of these patches in image space were tracked through the desired sequence of subsequent images. The resulting coordinates were later transformed from the image space to the physical space, with 30 pixels representing 10 mm. The PIVview software has a function for 'data smoothing' and all the test data were smoothed through this function, using 'median filtering'. Multigrid interrogation (grid refinement) was selected as the interrogation method. This allows a uniform pattern of displacement vectors to be output, using a least squares Gaussian fit for subpixel fitting, even though the speckle pattern is irregular.

6. Model validation

To validate the presented transparent soil model, initial tests were conducted with two cylindrical model piles, either flat tipped or with a 60° conical tip. These tests allowed comparison with theoretical predictions (CEM and SSPM) and other published experimental data (Cooke *et al.*, 1979; Francescon, 1983; Gue, 1984; Lehane and Gill, 2004; Ni *et al.*, 2010; Randolph *et al.*, 1979).

6.1 Comparison of the experimental results and SSPM predictions for circular pile penetration

Figure 8 shows measured displacement vectors around the model piles for $L/R = 10$ for the two cylindrical piles. The deformation patterns are consistent with previous published data. The rather small downward displacements below the pile tip are partly caused by lack of data directly below the model pile itself. Since the pixels should be square to avoid parallax effect (White *et al.*, 2003), a rectangular image zone was selected for PIV processing. The displacement vectors therefore start at a (final) radius of just over one times the pile radius (excluding the model pile itself), by which stage they are almost radial at the level of the pile tip, a transition between downward below the tip and upward above the tip.

The resulting displacement contours are presented in Figure 9 (flat tip) and Figure 10 (conical tip). Each figure shows separate plots for the normalised lateral (radial) displacement, u_r/R, and vertical displacement, u_z/R, at a penetration of $L/R = 10$.

Ni *et al.* (2010) presented SSPM numerical integration solutions for the displacement field around a 'simple pile' with a rounded tip. To allow for the 'effect of nose cone' reported by Ni *et al.* (2010), the appropriate SSPM solution is for $L/R = 12$, for comparison with the experimental results for $L/R = 10$. It was found

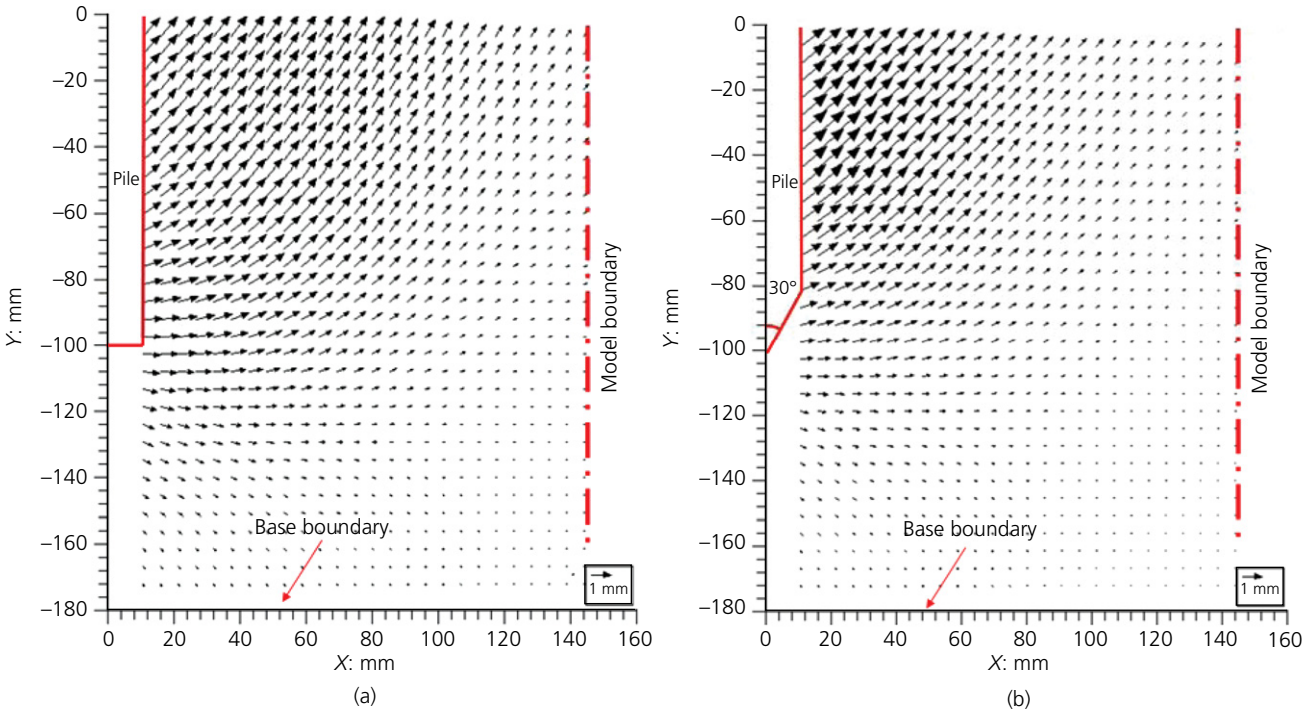

Figure 8. Displacement vectors around cylindrical model: (a) flat pile tip and (b) 60° tip

that reasonable agreement was achieved between the experimental results and the SSPM prediction (see Figures 6(c) and 6(d) in Ni *et al.*, 2010). However, there are some noticeable differences. The measured vertical displacement contours with $u_z/R = 0$ bend towards to the ground surface, while the predicted contours bend towards the model pile.

The difference between experimental and theoretical predictions is consistent with findings reported by Ni *et al.* (2010) and results from boundary effects. The SSPM solution is based on the assumption that the pile is penetrated into an infinite half-space soil, while the transparent soil experiments are performed in a chamber of finite size. The rigid bottom-wall would have restrained the soil particles moving towards the bottom of the chamber. It was also found that the displacement contour patterns for the flat-tipped pile closely resemble those for the conical-tipped pile. Only slight differences occur adjacent to the pile shaft and the ground surface, although these may be partly due to the non-uniform distribution of laser speckle patterns in the transparent soil.

6.2 Comparison with the CEM solution and existing experimental data

The CEM solution (Cooke *et al.*, 1979; Randolph *et al.*, 1979) is a very simple and useful tool to predict the radial displacement field around a pile. Experimental data, both from previous work and the present tests (mid-depth, $z_0/R = 5$, for pile penetration of $L/R = 10$), are compared in Figure 11 with predicted radial displacements, normalised by the pile radius R. The variable r represents the radial position of the soil particle before pile installation.

Relatively good agreement among all case histories, and with the CEM solution, is apparent in spite of the range of experimental procedures, pile tip geometries and soil types. It is worth noting that the measured data near the pile shaft ($r/R \leq \sim 2$) from the present tests lie below the CEM prediction and other reported data. This may be due to a 'laser reflection effect' at the pile shaft, which influences the speckle pattern close to the pile shaft. When $r/R > 2$, the effect becomes negligible and the radial displacements closely match the CEM solution. The general agreement of numerous case histories indicated in Figure 11 also emphasises the relevance of CEM solution in spite of its very simple theory.

7. Test results and discussion

7.1 Displacement patterns around XCC model pile in horizontal plane

The XCC pile has a non-axisymmetric cross-section, in contrast to a cylindrical pile, so it is necessary to explore the

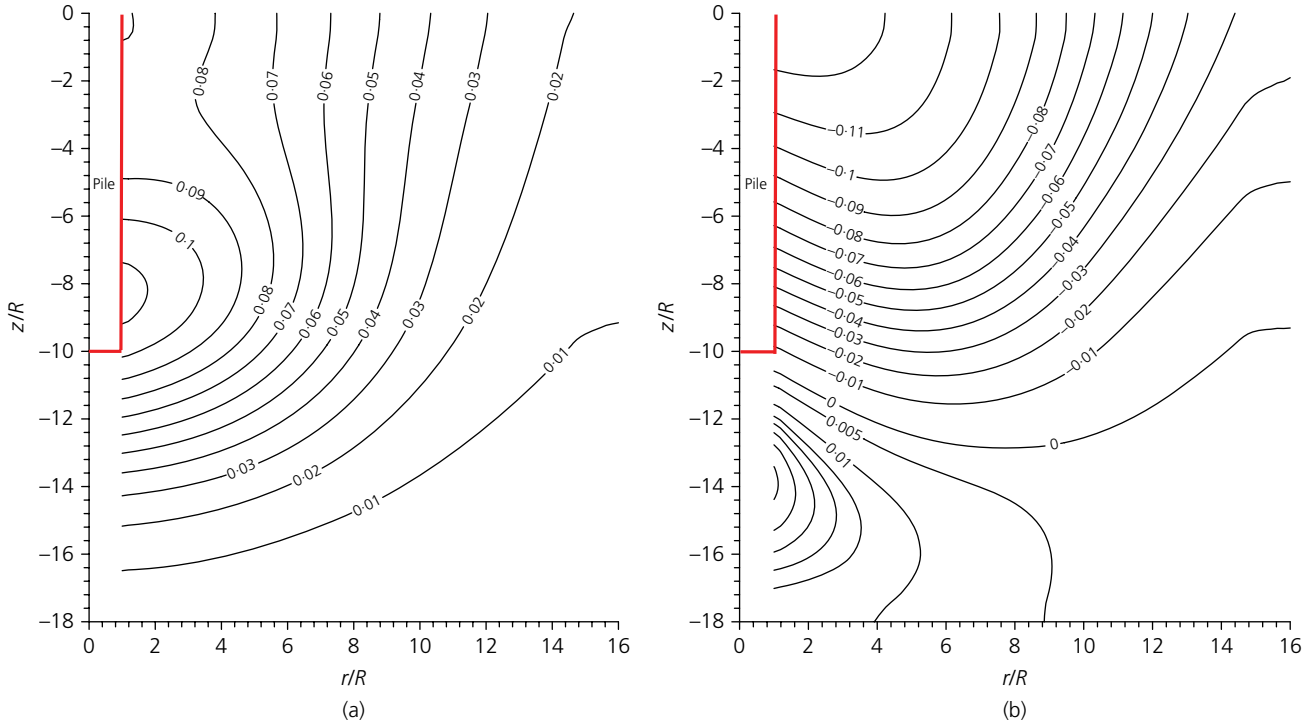

Figure 9. Normalised displacement contours for flat-tipped cylindrical pile at $L/R = 10$: (a) lateral and (b) vertical

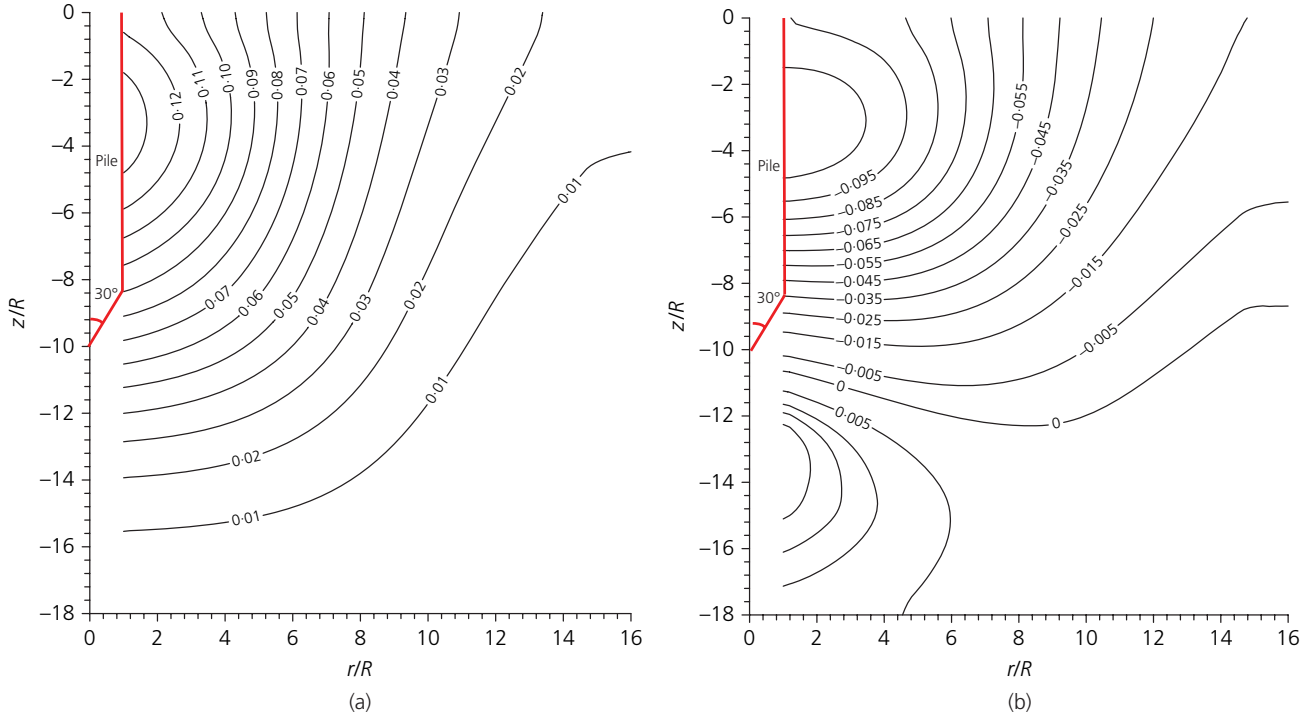

Figure 10. Normalised displacement contours for conical-tipped cylindrical pile at $L/R = 10$: (a) lateral and (b) vertical

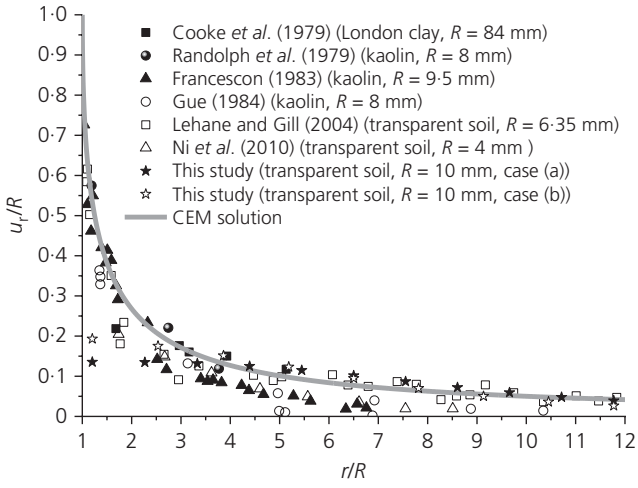

Figure 11. Comparison between CEM predictions and experimental data

applicability of the cylindrical cavity expansion model. In this section, the outward soil displacements around the XCC model pile are investigated through vector and contour plots in different horizontal planes, where the transparent soil model is sliced optically by the laser light sheet. Note that out-of-plane displacements were not obtained in this case, but were investigated separately using vertically oriented light sheets (see later).

Figures 12 and 13 show, respectively, the vectors and contour plots for incremental radial displacements on horizontal planes at $z_0/R_{eq} = 5$, 8, 9 and 10, following pile penetration from $L/R_{eq} = 0$ to 10.The horizontal and vertical axes represent the x-axis and y-axis, respectively, parallel to the maximum dimensions of the XCC cross-section. The anticipated four-fold symmetry is not quite obtained, reflecting some inaccuracies in the PIV data due to diffusion of the light source. The vectors (Figure 12) appear broadly to radiate from the pile axis.

From the contour diagrams (Figure 13), there appear to be two zones around the XCC pile: an inner transition zone and an outer cylindrical cavity expansion zone. In the transition zone, the displacements near the pile must accommodate the XCC shape, but transition gradually towards a more cylindrical pattern. This means that, in the cylindrical expansion zone, all field variables (displacements, strains, stresses and pore pressures) can be estimated using conventional CEM. The radius of the transition zone (i.e. distance from the dividing

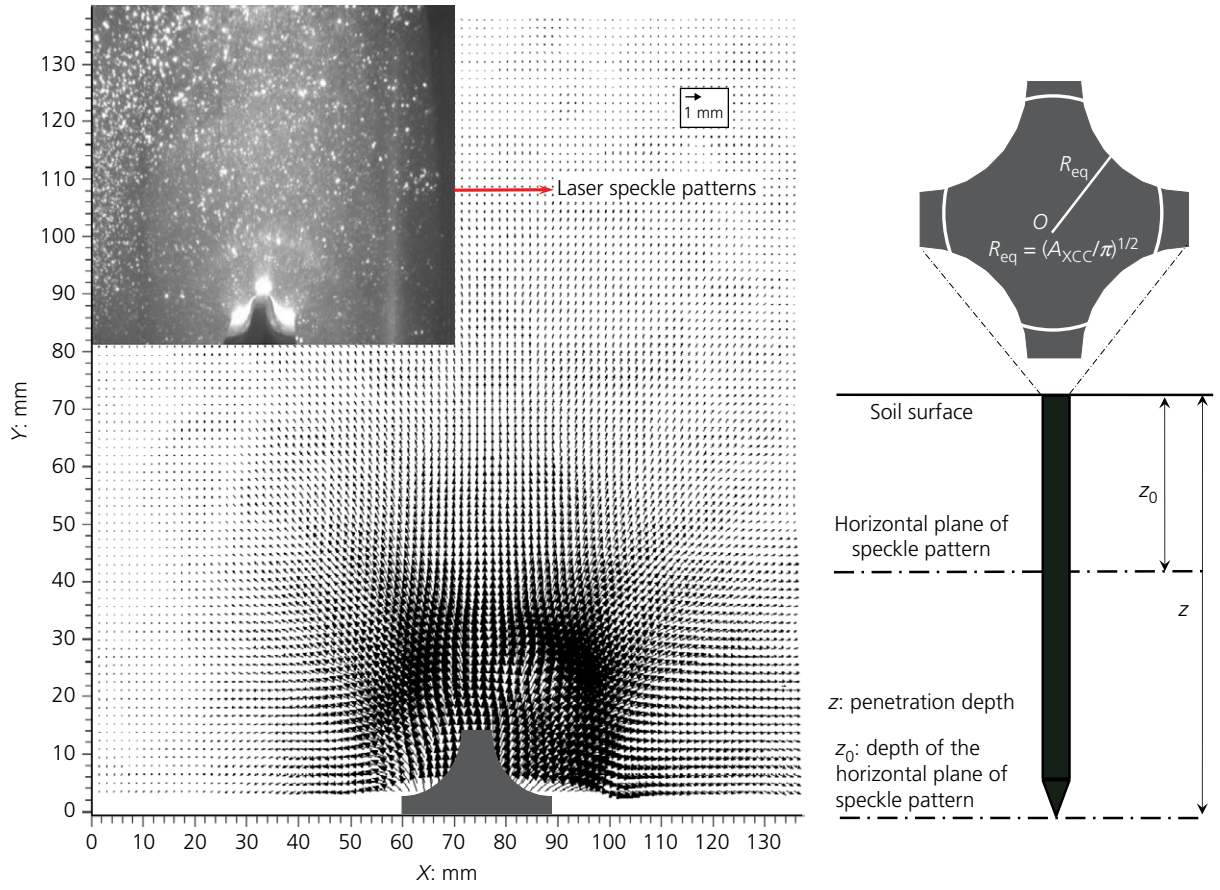

Figure 12. Displacement vectors and laser speckle patterns around XCC pile for penetration from $L/R_{eq} = 0$ to 10 in the horizontal plane at $z_0/R = 5$

line to the pile axis) is about 1·5 times the maximum dimension a of the XCC pile cross-section.

7.2 Displacement patterns around the XCC model pile in the vertical plane

Displacement patterns around the XCC model pile were also obtained on two vertical planes at 0° (profile A) and 45° (profile B) to the x and y axes. The displacement vectors are shown in Figure 14 for pile penetration from $L/R_{eq} = 0$ to 10. The general pattern is similar to that for a cylindrical pile (Figure 8(b)), although with differences in displacement magnitude.

The corresponding contours of radial and vertical displacement, normalised by the equivalent pile radius R_{eq}, are shown in Figure 15 (profile A) and Figure 16 (profile B). Comparing these figures, it can be clearly seen that the radial and vertical displacements in profile A are larger than those in profile B, as would be expected. The differences reduce significantly beyond a radius of about $5R_{eq}$, which is consistent with the transition zone radius of $1{\cdot}5a$ noted previously.

The results for the XCC pile can also be compared with those for the cylindrical pile, which has a cross-sectional area similar to A_{XCC}, and hence similar radius R to R_{eq}. Comparing Figure 15, Figure 16 and the corresponding Figure 10, it may be seen that the radial and vertical displacements in profile A are larger than for the cylindrical pile, while those for profile B are more similar.

8. The MCEM for XCC pile

The conventional cylindrical cavity expansion model is obviously unsuitable for the XCC pile penetration, as evident from the soil deformations observed in the transparent model tests. Mathematically, Equation 1 could not be applied in the vertical plane of profile B (at 45° to the direction of maximum pile width) because the final radial position of soil at the pile–soil interface would be less than the equivalent radius R_{eq}. Instead, an MCEM is proposed here to approximate the soil displacements around an XCC pile. The MCEM allows a transition between the X-shaped boundary at the pile–soil interface and cylindrical cavity

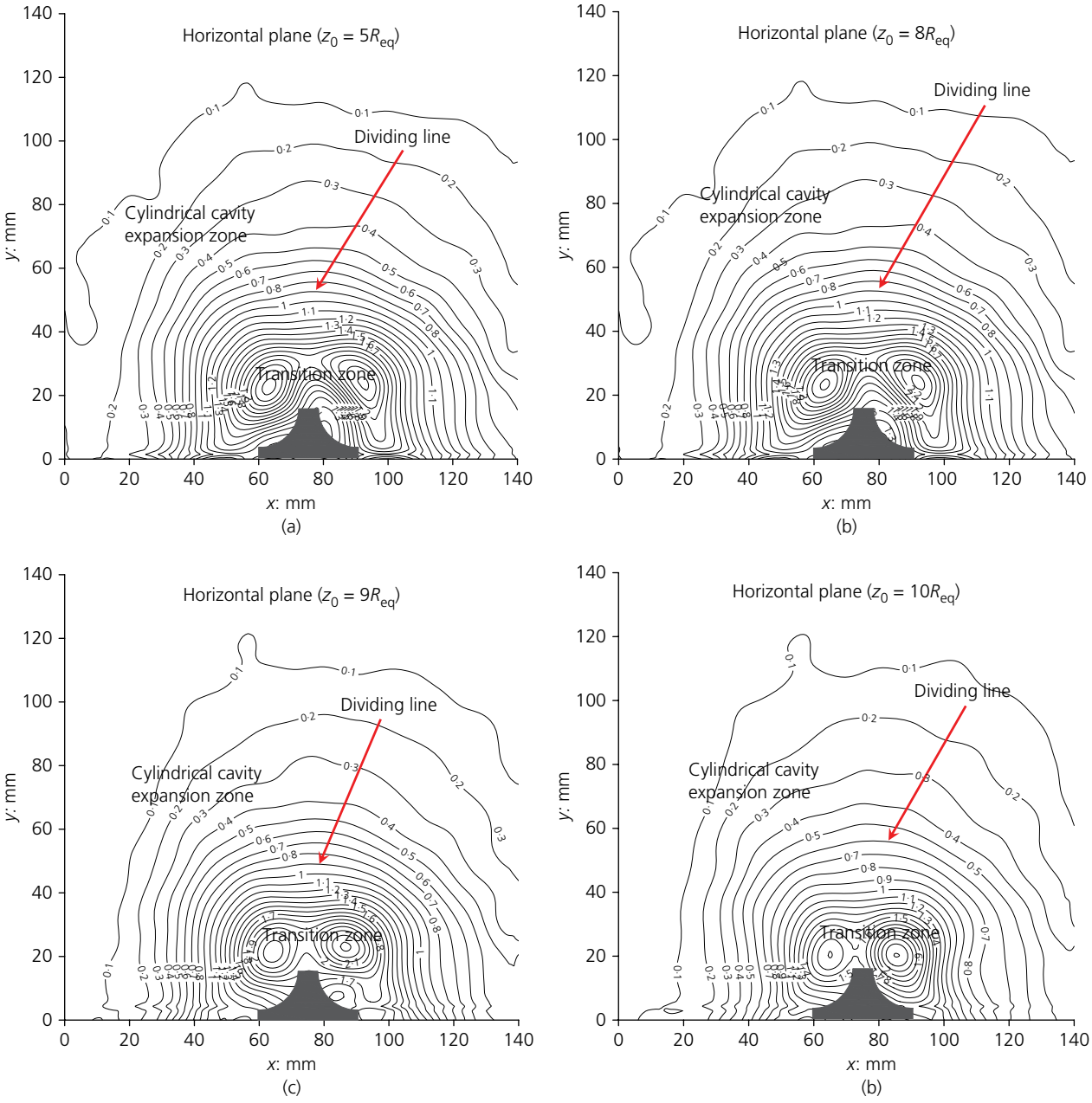

Figure 13. Displacement contours around the XCC pile in horizontal planes for penetration from $L/R_{eq} = 0$ to 10 in horizontal planes: (a) $z_0/R_{eq} = 5$, (b) $z_0/R_{eq} = 8$, (c) $z_0/R_{eq} = 9$, (d) $z_0/R_{eq} = 10$

expansion in the far field. It is based on the following two assumptions, which are consistent with the transparent soil model tests.

(*a*) the radius of the transition zone is $R_t = 1{\cdot}5a$
(*b*) the soil displacements are radially outwards from the pile axis in both the transition and cylindrical cavity expansion zones.

Figure 17 shows the new cavity expansion model. Two zones (transition zone of radius R_t and cylindrical cavity expansion) surround the XCC pile. It is convenient to introduce a polar coordinate system in addition to the Cartesian coordinate system, as shown, with coordinate origins located at the centre of the XCC pile cross-section. The x-axis and the y-axis are parallel to the maximum dimensions of the XCC pile, and correspond to $\theta = 0$ and 90° for the polar coordinates.

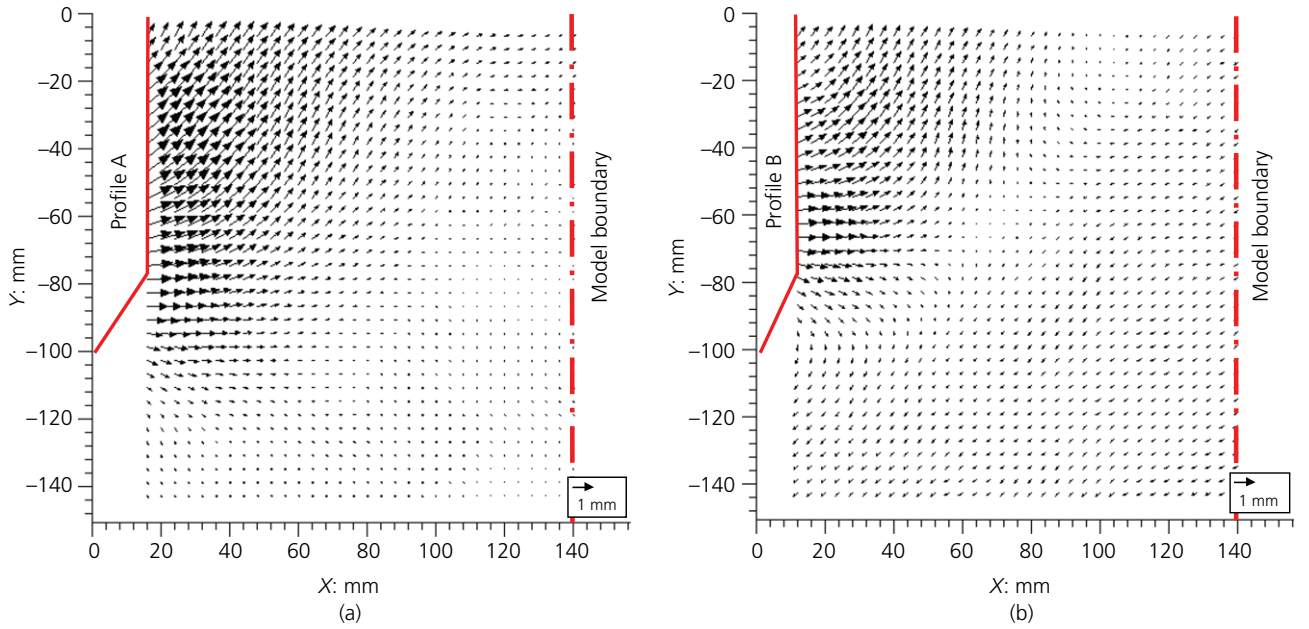

Figure 14. Displacement vectors for XCC pile: (a) profile A and (b) profile B

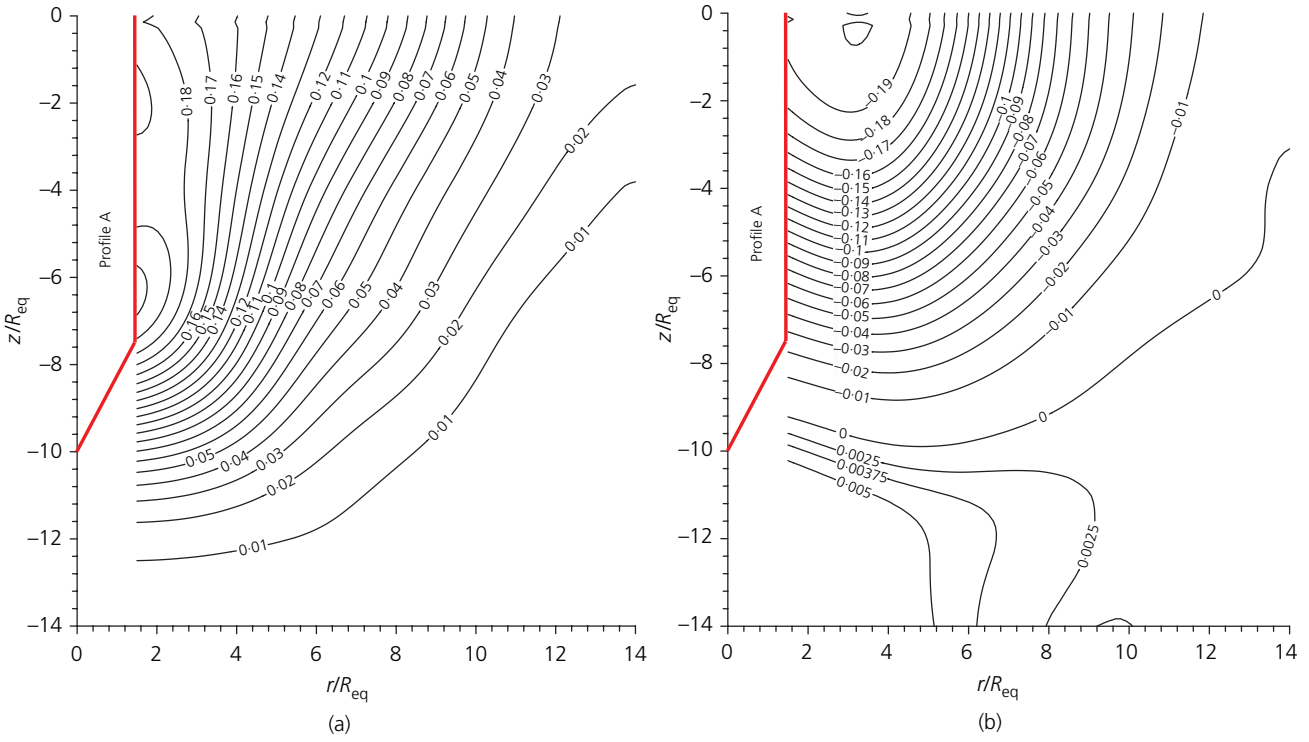

Figure 15. Normalised displacement contours for XCC pile (profile A) at $L/R_{eq} = 10$: (a) lateral and (b) vertical

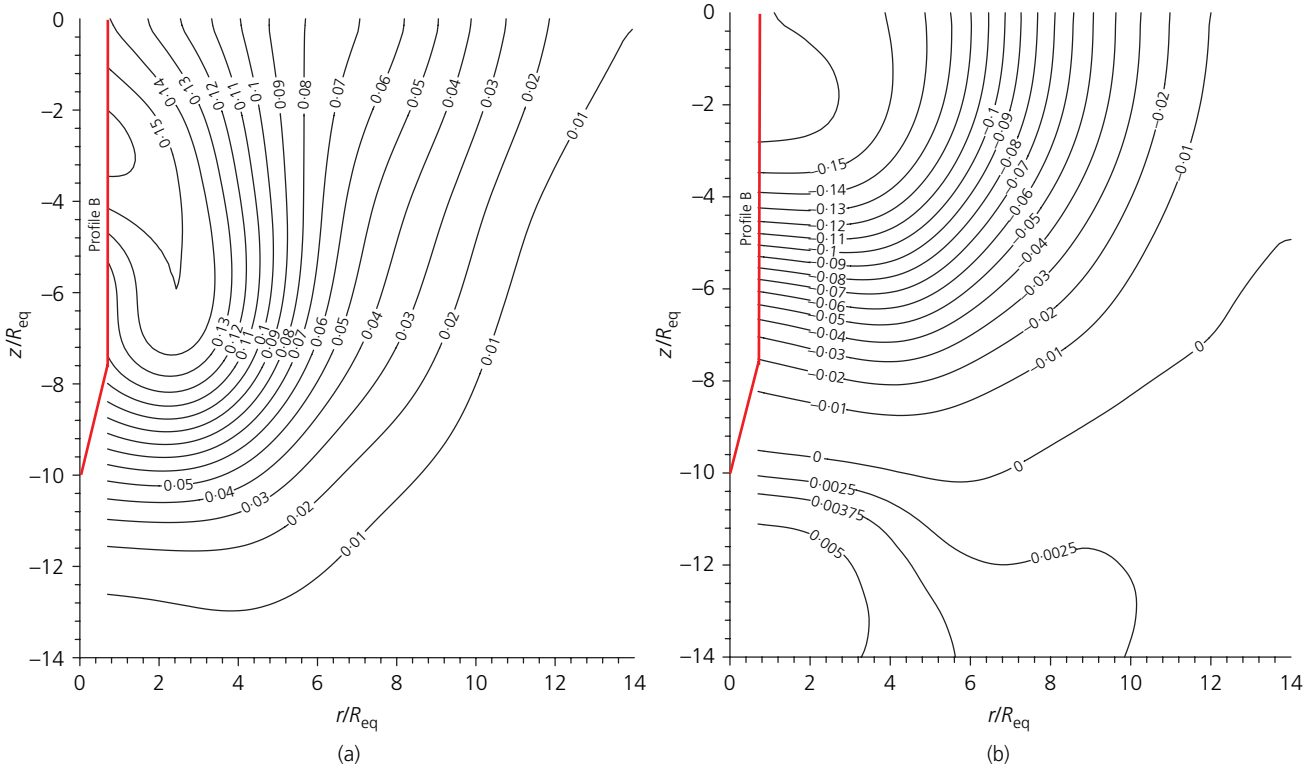

Figure 16. Normalised displacement contours for XCC pile (Profile B) at $L/R_{eq} = 10$: (a) lateral and (b) vertical

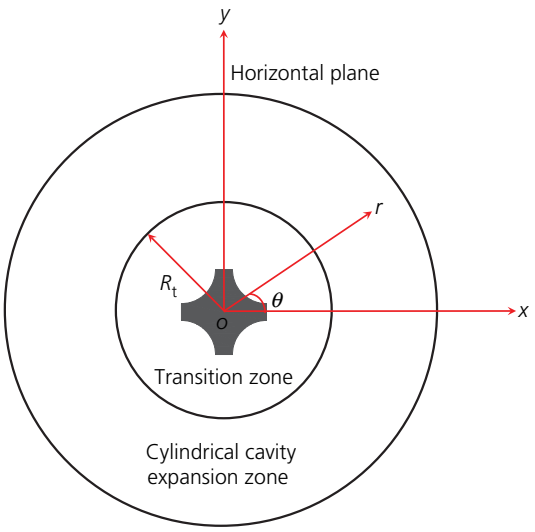

Figure 17. Modified cavity expansion model

8.1 Radial displacement

The displacements in the transition zone need to encompass the required variation with the polar angle due to the XCC shape, and also the need to become uniform (independent of the polar angle) at the transition limit of R_t. This may be achieved using a function for the radial displacements in the form

$$\frac{u_r}{r_0(\theta)} = \left(\frac{r_0(\theta)}{r}\right)^{n(\theta)} \quad (3)$$

where u_r is the radial displacement; $r_0(\theta)$ is the radius of the pile wall at angle θ; r is the final radial position of the soil particle; and $n(\theta)$ is a power that also varies with the polar angle. Note that this equation automatically guarantees that $u_r = r_0$ at the edge of the pile. The radius $r_0(\theta)$ at the pile–soil interface can be calculated according to the geometry of the XCC pile cross-section as detailed in the Appendix.

It is now necessary to determine the variable n from the condition at the edge of the transition zone, where the radial displacement, u_{rt}, at $r = R_t$ must be independent of θ and must satisfy the volume requirement that

$$\begin{aligned} u_{rt} &= R_t - \sqrt{R_t^2 - A_{XCC}/\pi} \\ &= R_t - \sqrt{R_t^2 - R_{eq}^2} \end{aligned} \quad (4)$$

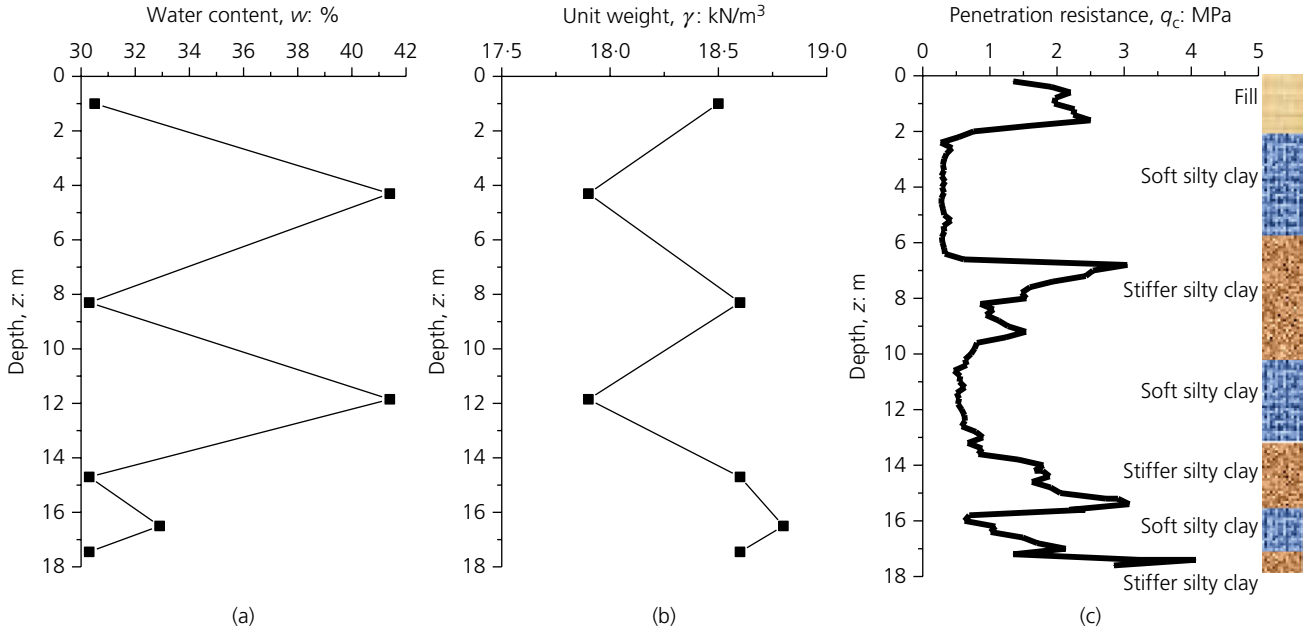

Figure 18. Site stratigraphy: (a) water content, (b) unit weight, (c) CPT data

Thus, substituting this condition into Equation 5 results in

$$5. \quad \frac{u_{rt}}{R_t} = \left(\frac{r_0}{R_t}\right)^{n+1} = 1 - \sqrt{1 - \left(R_{eq}/R_t\right)^2}$$

Taking the logarithm of both sides of this equation leads to

$$6. \quad n = \frac{-\ln\left(1 - \sqrt{1 - \left(R_{eq}/R_t\right)^2}\right)}{\ln(R_t/r_0)} - 1$$

The final expression of the radial displacement in the transition zone ($r < R_t$) can be written as

$$7. \quad \frac{u_r}{R_{eq}} = \left(\frac{r_0}{r}\right)^{n+1} \frac{r}{R_{eq}}$$

with both r_0 and n being functions of the polar angle θ. In the cylindrical cavity expansion zone ($r \geq R_t$), the radial displacement can be expressed as

$$8. \quad \frac{u_r}{R_{eq}} = \frac{r}{R_{eq}} - \sqrt{\frac{r^2}{R_{eq}^2} - 1}$$

It should be noted that there is a mild inconsistency in the assumption of purely radial flow, for typical XCC pile geometries where, in the notation of Appendix, the angle $\theta_1 = \arctan(b/a)$ is less than $\phi = \theta_0/2 - \pi/4$, since for a small part of the pile–soil interface strictly radial movement would involve passing through the pile. However, that region is quite limited ($\pi/4 - \arcsin\left(R_A/(2)^{1/2}x_A\right) < \theta < \phi$), and the required divergence from purely radial movement is slight.

9. Validation of the proposed MCEM solution

To verify the suitability of the proposed MCEM solution, the radial displacements predicted by MCEM were compared with the experimental results in this study and also field data. An instrumented field test was conducted in deltaic deposits of the Yangtze River near the site of the fourth bridge in Nanjing. In the field test, the displacements induced by XCC pile installation were measured and used subsequently to validate the proposed MCEM solution, particularly in respect of the radial displacements.

9.1 Description of the field test

The site stratigraphy, which comprised a 2 m thick layer of fill overlying a 4·6 m thick deposit of soft silty clay, is summarised in Figure 18. The soft silty clay is underlain by a 3·4 m thick deposit of stiffer silty clay, overlying 3·7 m thick soft silty clay. A 2 m thick deposit of stiffer silty clay is located between depth of 13·7 and 15·7 m, below which there is a 1·6 m thick

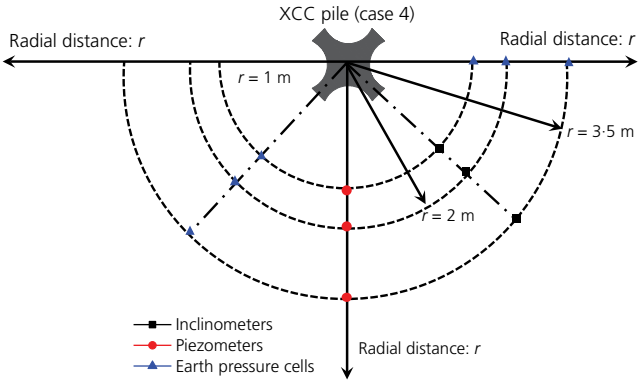

Figure 19. Plan view of instrumentation for the field test

deposit of soft silty clay extending down to 17·3 m and finally a deposit of stiffer silty clay. As shown in Figure 18, the water content of the deposit soil changes from 30to 42%, whereas the unit weight ranges from 17·8 to 18·7 kN/m^3 at different depths. In addition, the cone resistance varies between 0·3 MPa for the upper soft silty clay, and 3 MPa, for the stiffer silty clay. The water level is typically at a depth of 1·2 m, with slight seasonal fluctuations. The rigidity index (G/s_u) for the soft silty clay (for the relevant depth of $z = 3$ m and $z = 6$ m) has been estimated as about 100, while for the stiffer silty clay (at $z = 9$ m depth) it is 400. The undrained strengths of the soft and stiffer silty clays are estimated as 10 and 25 kPa, respectively, from the CPT data.

The XCC pile cross-section is defined by the three parameters: $a = 611$ mm, $b = 120$ mm, $\theta_0 = 130°$ (giving $R_{eq} = 210$ mm); it was driven to an embedment of 20 m. Figure 19 shows a plan view of the instrumentation arrangement around the XCC pile. This comprised three inclinometers, six piezometers and 12 earth pressure cells. As shown, the instrumentation was located at radial distances of 1, 2 and 3·5 m, and along the $\theta = 0°$ (inclinometers, earth pressure cells) and $\theta = 45°$ (piezometers, earth pressure cells) polar directions, and at depths of 3 and 6 m (piezometers and earth pressure cells). The measured pore pressure and earth pressure data are not presented in this paper, which focuses on the radial displacements derived from the inclinometer data. Note that the measurements were recorded directly after installation, which is consistent with the assumption of undrained conditions.

9.2 Comparison of predicted and measured radial displacements

The normalised radial displacements, u_r/R_{eq}, predicted by the MCEM and measured in laboratory and field, are plotted against the normalised final radius r/R_{eq} in Figure 20. Here, two groups of transparent soil test data (from the horizontal and vertical planes) are selected for comparison in Figures 20(a) and 20(b). The radial displacements predicted by the conventional CEM are also included for comparison. The transition zone for the MCEM has been taken as $R_t = 1{\cdot}5a = 4{\cdot}4R_{eq}$.

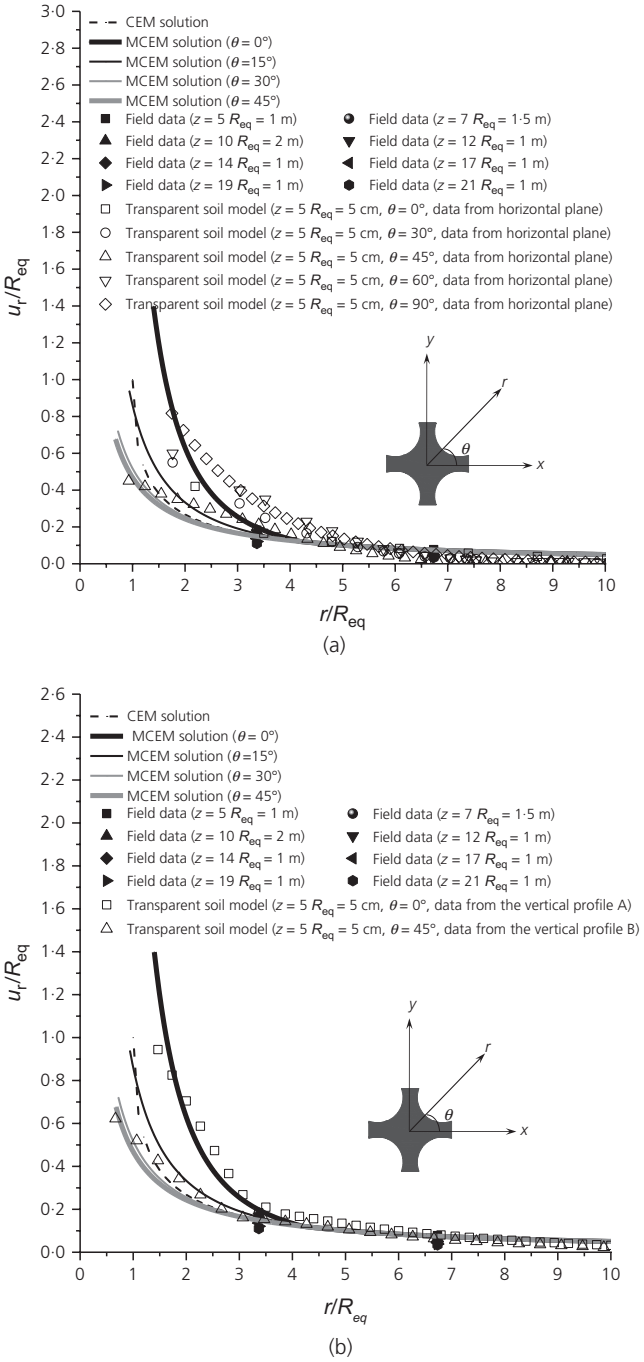

Figure 20. Comparison of normalised radial displacements predicted by CEM and MCEM with laboratory and field data: (a) horizontal planes and (b) vertical planes

The field data are only available at two discrete radii (and for $\theta = 0$), with the inner set of data just within the transition zone, but plotting closer to the simple cylindrical cavity expansion curve than to the relevant MCEM curve. This could imply a smaller width of the transition zone for the field conditions. For the transparent soil tests, Figure 20(b) shows a very reasonable match for the distribution of the radial displacements around the XCC pile in both the inner transition zone and the outer cylindrical expansion zone. By contrast, the transparent soil test data for the radial displacements in Figure 20(a) show rather different variations with radius than the theoretical curves. At intermediate radii, the measured displacements mostly lie above the corresponding MCEM curves, while in the outer cylindrical expansion zone the data lie below the theoretical prediction. This discrepancy is believed to be attributable to the lower accuracy of measurements in the horizontal plane compared with the vertical plane (see discussion below).

The comparison suggests that in the outer cylindrical cavity expansion zone either of the CEM and MCEM solutions (which are identical in that zone) can predict the radial displacements around the XCC pile very well. However, the CEM solution does not capture the much larger radial displacements for the $\theta = 0$ or 90° directions within the transition zone; the data in that zone are predicted much better using the MCEM solution.

9.3 Accuracy of the measurements on horizontal and vertical planes

The relative accuracy of the PIV data obtained using either vertically oriented or horizontally oriented planes of light is discussed here. It was found that the quality, and hence accuracy, of the digitised data from horizontal light planes was inferior to those from vertical light planes. In the model test, the camera was tied and positioned to the penetration axis above the pile when capturing the horizontal data. The lower accuracy of the horizontal data is mainly because the top model surface was not guaranteed to be perfectly horizontal for light to consistently exit the top of the model for imaging. This occurs because the camera was not sufficiently rigidly attached above the pile. Any lack of normality between the camera viewing direction and the soil surface will result in a parallax effect, as observed by White *et al*. (2003). A single scale factor is used to convert between pixel coordinates and object-space position (with a transformation relation of 30 pixels representing 1 cm for both the horizontal and vertical planes) according to Taylor *et al*. (1998) and Paikowsky and Xi (2000). However, the assumption of a single scale factor is valid only if the camera behaves according to the pinhole model, the object plane is exactly parallel to the CCD plane and the pixels are square (White *et al*., 2003). For the vertical data, the camera was positioned on stable equipment, perpendicular and central to the plane of measurement (Figure 7), which results in better resolution than the horizontal data.

10. Limitations

The transparent model test presented in this paper successfully captures the undrained displacement response during the XCC pile installation process, which shows the non-cylindrical mechanism of the XCC pile. The presented analysis provides a basis in the future for developing predictions of stress changes and, ultimately, shaft capacity of the XCC pile in comparison to displacement piles of circular cross-section. However, the presented test methods and results should be limited to the undrained cases of soil since the relatively large grain size of the used fused silica for transparent soil renders its response more like a sand than a clay, although this is compensated by the highly viscous nature of the oil (two to three orders of magnitude greater than water). In addition, the wire-cutting process used to fabricate the model XCC pile automatically led to a rough surface, with maximum roughness ~ 1 mm, which resulted in a 'fully rough' interface.

11. Conclusions

In this study, a transparent soil model was used to investigate the soil displacement patterns arising from installation of a new type of pile, the cast in-situ XCC pile, which has a non-symmetrical shape in cross-section with eight-fold symmetry. The soil displacements within the transparent soil were evaluated using a laser light source to create a speckle pattern on particular planes, and then using PIV techniques to quantify changes in the location of a given speckle pattern due to pile installation. The technique was first trialled using a simple cylindrical pile, comparing the measured radial soil displacements with predictions from cavity expansion and SPMs. The technique was then used for a model XCC pile, collecting data on horizontal planes at different depths within the model, and also vertical planes through the pile axis, oriented parallel to either the maximum or the minimum cross-sectional dimensions of the pile. Soil displacement data from the laboratory tests were supplemented by inclinometer data from a field test conducted in deltaic deposits of the Yangtze River near the site of the fourth bridge in Nanjing.

The following main conclusions may be drawn with respect to soil displacements arising from installation of the XCC pile mould.

- Overall, the pattern of soil displacements is similar to that for a cylindrical pile, with primarily radial displacements around the pile shaft, but with distinctly smaller displacements in the vertical plane through the narrowest section of the pile. In the far field, beyond a radius of

about 1·5 times the maximum width of the pile, the displacements become essentially axisymmetric. However, closer to the pile, within what is termed a transition zone, the magnitude of radial displacements reflect the variation in local radius (or semi-width) of the pile with the polar angle.
- On the basis of these observations, an MCEM was developed to allow prediction of radial soil displacements for any polar angle.
- Predictions using the MCEM showed reasonable agreement with the data from both the transparent soil tests and the field test.

A final comment is relevant concerning the relative accuracy of the PIV data obtained using either vertically oriented or horizontally oriented planes of light. It was found that the quality, and hence accuracy, of the digitised data from the horizontal light planes was inferior to those from vertical light planes.

Acknowledgements

The work was supported by the National Natural Science Foundation of China (numbers 51478165 and 51420105013), and the 111 Project (number B13024). The first author was hosted as a PhD student at the Centre for Offshore Foundation Systems (COFS) during part of this work. COFS is currently supported as a node of the Australian Research Council's Centre of Excellence for Geotechnical Science and Engineering (CE110001009), and through the Fugro Chair in Geotechnics, the Lloyd's Register Foundation Chair and Centre of Excellence in Offshore Foundations and the Shell EMI Chair in Offshore Engineering.

Appendix: Derivation of radial distance to pile–soil interface

Figure 21 shows detailed geometric relations for the XCC pile cross-section. Due to the eight-fold symmetry, the XCC pile cross-section may be divided into 16 distinct areas, although it is convenient algebraically to consider the three areas indicated in any given quadrant of the pile. Areas 1 and 3 represent flat sections of the cross-section (and are mirror images of each other), whereas area 2 refers to the cambered section. It should also be noted that, in practice, the angle $\theta_0 \geq \pi/2$. The radial distance to the pile–soil interface is derived below for each of these areas.

Areas 1 and 3

In area 1, the radial distance is simply

$$9. \quad r_0 = \frac{a}{2\cos\theta}$$

Analogously, in area 3 the radial distance is

$$10. \quad r_0 = \frac{a}{2sin\theta}$$

Area 2

The coordinates of point A (the centre of the arc) can be written in rectangular coordinates as

$$11a. \quad x_A = y_A = \frac{a}{2} - R_A \sin\varphi$$

where R_A is the radius of the arc and the angle φ is given by

$$11b. \quad \varphi = \frac{\theta_0}{2} - \frac{\pi}{4}$$

Noting that

$$12. \quad R_A(\cos\phi + \sin\phi) + \frac{a}{2}\tan\theta_1 = \frac{a}{2}$$

the arc radius, R_A, can be expressed as

$$13a. \quad R_A = k_1 a$$

where

$$13b. \quad k_1 = \frac{1 - \tan\theta_1}{2(\sin\varphi + \cos\varphi)}$$

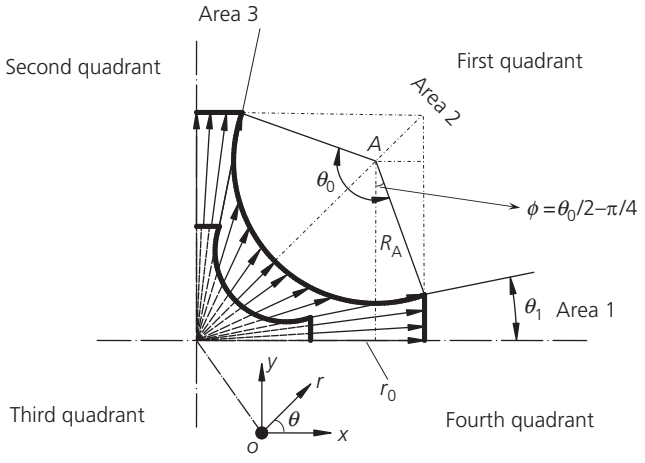

Figure 21. Geometric details of XCC pile cross-section

Substituting Equation 13 into Equation 11 results in

$$14a. \quad x_A = y_A = k_2 a$$

where

$$14b. \quad k_2 = \frac{1}{2} - k_1 \sin\varphi$$

In addition, the equation of the arc (cambered section) is

$$15. \quad (x - x_A)^2 + (y - y_A)^2 = R_A^2$$

In cylindrical coordinates, Equation 15 can be written as

$$16. \quad r_0^2 - 2r_0(x_A \cos\theta + y_A \sin\theta) + x_A^2 + y_A^2 - R_A^2 = 0$$

where r_0 is the radial position at the pile–soil interface.

Equation 16 is a quadratic equation with respect to the variable r_0, with the smaller root expressed as

$$17. \quad r_0 = a\left[k_2(\cos\theta + \sin\theta) - \sqrt{k_2^2(\cos\theta + \sin\theta)^2 - (2k_2^2 - k_1^2)}\right]$$

Total cross-sectional area

The total cross-sectional area of the XCC pile may be calculated as

$$18. \quad A_{XCC} = \frac{a^2 - 2b^2 + 2b\sqrt{a^2 - b^2}}{2} - \left(a^2 - 2b\sqrt{a^2 - b^2}\right)\frac{\theta - \sin\theta}{4\sin^2(\theta/2)}$$

REFERENCES

Ahmed M and Iskander M (2010) Analysis of tunnelling-induced ground movements using transparent soil models. *Journal of Geotechnical and Geoenvironmental Engineering* **137(5)**: 525–535.

Baligh MM (1985) Strain path method. *Journal of Geotechnical Engineering* **111(9)**: 1108–1136.

Cao LF, Teh CI and Chang MF (2001) Undrained cavity expansion in modified Cam clay I: theoretical analysis. *Géotechnique* **51(4)**: 323–334, https://doi.org/10.1680/geot.2001.51.4.323.

Carter JP, Booker JR and Yeung SK (1986) Cavity expansion in cohesive frictional soils. *Géotechnique* **36(3)**: 345–358, https://doi.org/10.1680/geot.1986.36.3.349.

Chen SL and Abousleiman YN (2012) Exact undrained elasto-plastic solution for cylindrical cavity expansion in modified Cam Clay soil. *Géotechnique* **62(5)**: 447–456, https://doi.org/10.1680/geot.11.P.027.

Cooke RW, Price G and Tarr K (1979) Jacked piles in London Clay: a study of load transfer and settlement under working conditions. *Geotechnique* **29(2)**: 113–147, http://dx.doi.org/10.1680/geot.1979.29.2.113.

Ezzein FM and Bathurst RJ (2011) A transparent sand for geotechnical laboratory modeling. *Geotechnical Testing Journal* **34(6)**: 590–601.

Francescon M (1983) *Model Pile Tests in Clay: Stresses and Displacements Due to Installation and Axial Loading*. PhD thesis, University of Cambridge, Cambridge, UK.

Gibson RE and Anderson WF (1961) In situ measurement of soil properties with the pressuremeter. *Civil Engineering Public Works Review* **56(658)**: 615–618.

Gue SS (1984) *Ground Heave around Driven Piles in Clay*. PhD thesis, University of Oxford, Oxford, UK.

Guzman IL and Iskander M (2013) Geotechnical properties of sucrose-saturated fused quartz for use in physical modeling. *Geotechnical Testing Journal* **36(3)**: 448–454.

Hill R (1950) *The Mathematical Theory of Plasticity*. Oxford University Press, London, UK.

Hird CC, Ni Q and Guymer I (2011) Physical modelling of deformations around piling augers in clay. *Geotechnique* **61(11)**: 993–999, http://dx.doi.org/10.1680/geot.9.T.028.

Iskander M, Lai J, Oswald C and Mannheimer R (1994) Development of a transparent material to model the geotechnical properties of soils. *ASTM Geotechnical Testing Journal, GTJODJ* **17(4)**: 425–433.

Lehane BM and Gill DR (2004) Displacement fields induced by penetrometer installation in an artificial soil. *International Journal of Physical Modelling in Geotechnics* **4(4)**: 25–36, http://dx.doi.org/10.1680/ijpmg.2004.040103.

Liu J and Iskander M (2004) Adaptive cross correlation for imaging displacements in soils. *Journal of Computing in Civil Engineering* **18(1)**: 46–57.

Liu HL, Zhou H and Kong G (2014) XCC pile installation effect in soft soil ground: A simplified analytical model. *Computers and Geotechnics* **62**: 268–282.

Lorenz H and Heinz WF (1969) Change of density in sands due to loading. *Proceedings of 7th International Conference on Soil Mechanics and Foundation Engineering*, vol. 1. Sociedad Mexicana de Mecanica, Mexico City, Mexico, pp. 267–273.

Lv Y, Liu H, Ding X and Kong G (2011) Field tests on bearing characteristics of X-section pile composite foundation. *Journal of Performance of Constructed Facilities* **26(2)**: 180–189.

Lv Y, Liu H, Ng CW, Ding X and Gunawan A (2014a) Three-dimensional numerical analysis of the stress transfer mechanism of XCC piled raft foundation. *Computers and Geotechnics* **55**: 365–377.

Lv Y, Liu H, Ng CW, Gunawan A and Ding X (2014b) A modified analytical solution of soil stress distribution for XCC pile foundations. *Acta Geotechnica* **9(3)**: 529–546.

Mandava SS, Watson AT and Edwards CM (1990) NMR imaging of saturation during immiscible displacements. *AIChE Journal* **36(11)**: 1680–1686.

Ni Q, Hird CC and Guymer I (2010) Physical modelling of pile penetration in clay using transparent soil and particle image velocimetry. *Geotechnique* **60(2)**: 121–132, http://dx.doi.org/10.1680/geot.8.P.052.

Orsi TH, Anderson AL, Leonard JN, Bryant WR and Edwards CM (1992) Use of X-ray computed tomography in the study of marine sediments. *Proceedings, CEOV*. ASCE, College Station, TX, USA, pp. 968–982.

Paikowsky S and Xi F (2000) Particle motion tracking utilizing a high-resolution digital CCD camera. *Geotechnical Testing Journal* **23(1)**: 123–134.

Posadas DAN, Tannus A, Panepucci H and Crestana S (1996) Magnetic resonance imaging as a non-invasive technique for investigating 3-d preferential flow occurring within stratified soil samples. *Computers and Electronics in Agriculture* **14(4)**: 255–267.

Randolph MF, Carter JP and Wroth JR (1979) Driven piles in clay-the effects of installation and subsequent consolidation. *Géotechnique* **29(4)**: 361–393, https://doi.org/10.1680/geot.1979.29.4.361.

Roscoe K, Arthur J and James R (1963) The determination of strains in soils by an X-ray method. *Civil Engineering and Public Works Review* **58(873–876)**: 1009–1012.

Sagaseta C, Whittle AJ and Santagata M (1997) Deformation analysis of shallow penetration in clay. *International Journal for Numerical and Analytical Methods in Geomechanics* **21(10)**: 687–719.

Sadek S, Iskander M and Liu J (2003) Accuracy of digital image correlation for measuring deformations in transparent Media. *Journal of Computing in Civil Engineering* **17(2)**: 88–96.

Salgado R, Mitchell JK and Jamiolkowski M (1997) Cavity expansion and penetration resistance in sand. *Journal of Geotechnical and Geoenvironmental Engineering* **123(4)**: 344–354.

Taylor RN, Grant RJ, Robson S and Kuwano J (1998) An image analysis system for determining plane and 3-D displacements in soil models. *Proceedings of Centrifuge '98*, Balkema, Rotterdam, pp. 73–78.

Vesic AC (1972) Expansion of cavities in infinite soil mass. *Journal of the Soil Mechanics and Foundations Division ASCE* **98(SM3)**: 265–290.

Welker A, Bowders J and Gilbert R (1999) Applied research using transparent material with hydraulic properties similar to soil. *ASTM Geotechnical Testing J.* **22(3)**: 266–270.

White DJ, Take WA and Bolton MD (2003) Soil deformation measurement using particle image velocimetry (PIV) and photogrammetry. *Geotechnique* **53(7)**: 619–631, http://dx.doi.org/10.1680/geot.2003.53.7.619.

Willert C (2015) *PIVview 2C/3C User Manual Version 2.3*. Göttingen, Germany.

Yu HS (1990) *Cavity Expansion Theory and Its Application to the Analysis of Pressuremeters*. PhD thesis, University of Oxford, Oxford, UK.

Zhou H, Liu H, Kong G and Cao Z (2014a) Analytical solution for pressure-controlled elliptical cavity expansion in elastic-perfectly plastic soil. *Geotechnique letters* **4(April–June)**: 72–78, https://doi.org/10.1680/geolett.14.00004.

Zhou H, Liu H and Kong G (2014b) Influence of shear stress on cylindrical cavity expansion in undrained elastic–perfectly plastic soil. *Geotechnique letters* **4(July–September)**: 203–210, https://doi.org/10.1680/geolett.14.00034.

Zhou H, Liu H, Kong G and Huang X (2014c) Analytical solution of undrained cylindrical cavity expansion in saturated soil under anisotropic initial stress. *Computers and Geotechnics* **55**: 232–239.

Zhou H, Kong G, Li P and Liu H (2015) Flat cavity expansion: theoretical model and application to the interpretation of the flat dilatometer test. *Journal of Engineering Mechanics* **142(1)**: 04015058.

How can you contribute?

To discuss this paper, please email up to 500 words to the editor at journals@ice.org.uk. Your contribution will be forwarded to the author(s) for a reply and, if considered appropriate by the editorial board, it will be published as discussion in a future issue of the journal.

International Journal of Physical Modelling in Geotechnics relies entirely on contributions from the civil engineering profession (and allied disciplines). Information about how to submit your paper online is available at www.icevirtuallibrary.com/page/authors, where you will also find detailed author guidelines.